Switching of control mechanisms during the rapid solidification of a melt pool

Yijia Gu [1], Jiandong Yuan,[2,3] and Lianyi Chen [2,3]

[1]Department of Materials Science and Engineering, Missouri University of Science and Technology, Rolla, Missouri 65409, USA
[2]Department of Mechanical Engineering, University of Wisconsin-Madison, Madison, Wisconsin 53706, USA
[3]Department of Materials Science and Engineering, University of Wisconsin-Madison, Madison, Wisconsin 53706, USA

(Received 18 May 2023; accepted 11 September 2023; published 3 October 2023; corrected 14 November 2023)

The solidification of alloys is typically controlled by solute diffusion due to the solute partitioning happening at the solid-liquid interface. In this study, we show that the switching from solute diffusion-controlled growth to thermal diffusion-controlled growth may happen at the solidification front during rapid solidification processes of alloys such as additive manufacturing using a phase-field model. The switching is found to be triggered by the cooling of the solid-liquid interface when it becomes colder than the solidus temperature. The switching introduces a sudden jump of growth velocity, an increase in solute concentration, and the refining of the resulting microstructures. All those changes predicted by the phase-field simulations agree with experimental observations quantitatively. The switching of control mechanisms can be exploited by manipulating the processing conditions to form refined microstructures or layered structures for improved mechanical properties.

DOI: 10.1103/PhysRevMaterials.7.103401

I. INTRODUCTION

Metals and alloys is one of the most important families of structural materials due to their superior mechanical properties, such as high strength, high stiffness, and good ductility. The process of their solidification remains a crucial area of investigation. The spontaneous pattern formation in the growth of crystals during the solidification of metals and alloys is intriguing in nature. It is one example of those self-organizing systems studied by scientists for years [1]. The microstructure developed during solidification is vital for metallic products as it is the starting point of the following solid-state manufacturing processes. Specifically, it dictates the selection of metal-forming processes, the design of heat treatment, and a few final properties of the product.

The solidification of metals and alloys is a complex process. Microscopically, solidification proceeds by the movement of the solid-liquid interface, accompanied by the change of interfacial curvature, the release of latent heat, and the partitioning of solute atoms (for alloys). The growth of the solid phase is controlled by the diffusion fields in the neighborhood of the solid-liquid interface. Thermal diffusion controls the solidification growth in pure metals. The interface propagates as the latent heat dissipates. In alloys, the interface kinetics is complicated by the partitioning of the solute elements across the solid-liquid interface, which is a much slower diffusion process than thermal diffusion. Therefore, although the solidification process of alloys also involves the production of substantial latent heat, the interface is typically controlled by solute diffusion.

Reversely, the interface velocity influences the thermal diffusion and solute diffusion by generating the latent heat and changing the solute partition, respectively. The production rate of latent heat is proportional to interface velocity. Higher interface velocity leads to a heated interface. Solute partitioning is also affected by interface velocity but in a complex manner. For dilute alloys, the dependence of partition coefficient k, the ratio of solute concentration in the solid (c_s) to that in the liquid (c_l), on the interface velocity v_n is given by [2]

$$\begin{cases} k = \dfrac{k_e\left[1-\left(\frac{v_n}{v_D}\right)^2\right]+\frac{v_n}{v_D}}{1-\left(\frac{v_n}{v_D}\right)^2+\frac{v_n}{v_D}}, & v_n < v_D, \\ k = 1, & v_n \geqslant v_D \end{cases} \tag{1}$$

where k_e is the equilibrium partition coefficient, v_n is the interface velocity, $v_D = D_l/\delta$ is the interface diffusion velocity, D_l is the diffusivity of the solute in the liquid, and δ is the atomic jump distance in the liquid. For metals and alloys, v_D is on the magnitude of 10 m/s [3,4]. For small velocity ($v_n \ll v_D$), the partition coefficient can be approximated using the continuous-growth model [5,6], i.e.,

$$k = \left(k_e + \frac{v_n}{v_D}\right)\Big/\left(1+\frac{v_n}{v_D}\right). \tag{2}$$

When the interface velocity is high enough, partial or no solute partitioning may happen. This phenomenon is called solute trapping [7]. In the case of complete solute trapping ($k = 1$), the interface of the solidifying alloy is controlled by thermal diffusion alone.

To facilitate the discussion, the thermodynamics of solidification is briefly analyzed below following Baker and Cahn [8]. Figure 1 shows a schematic phase diagram (lower panel) and its corresponding molar Gibbs free energies of solid (α) and liquid (L) phases at temperature T_P (upper panel) of an A-B dilute alloy. The phase diagram is divided into four regions: liquid, region I, region II, and α (region III). Regions I and II make up the α+liquid two-phase field and are separated by the so-called T_0 line. The T_0 line denotes where the molar Gibbs free energy of the liquid and that of α are equal. The complete solute trapping and steady-state growth are only

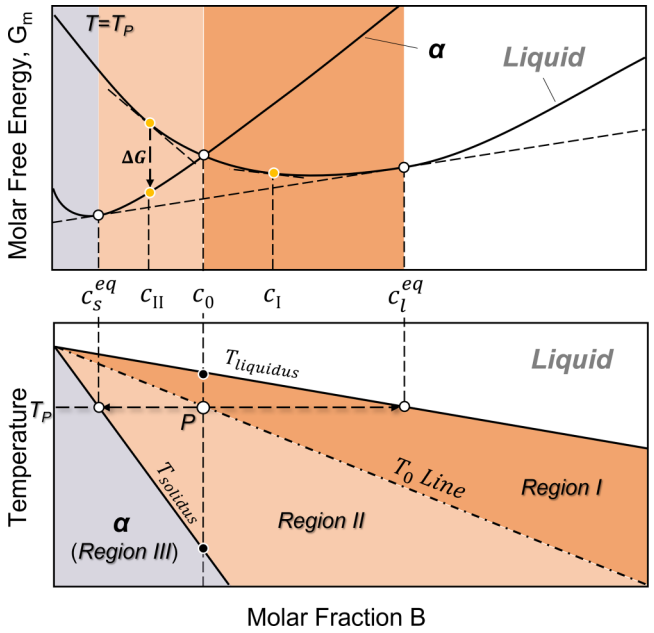

FIG. 1. Phase diagram of dilute alloy and its Gibbs free-energy curves at $T = T_P$. T_0 denotes where molar Gibbs free energy of liquid phase and solid (α) phase are equal. Liquidus, solidus, and T_0 line defining three regions.

allowed in region II and region III (single α-phase region) [8]. In region II, a high interface velocity ($\geqslant v_D$) is required to achieve complete solute trapping as the solute partitioning is energetically favored. However, in region III, partitioning is no longer thermodynamically required. When the interface gets into this region, it becomes thermal diffusion controlled automatically no matter how slow it moves. Generally, when the interface temperature drops below solidus and gets into region III, the undercooling is exceptionally large, and the interface velocity is correspondingly high. In summary, there are two scenarios where the solidification of an alloy can be completely controlled by thermal diffusion: (1) the interface lies in region II and its velocity is high enough ($\geqslant v_D$), or (2) the interface lies in single α-phase region (below solidus).

The existence of the switching between solute diffusion-controlled growth and thermal diffusion-controlled growth in the solidification of alloys has been confirmed experimentally. Evidence for thermal diffusion-controlled alloy solidification was demonstrated by electromagnetic levitation experiments [9,10]. With the changing initial undercooling, the solidification growth velocity was found to change accordingly. At a critical undercooling, a sudden rise in the growth velocity is observed. Partitionless solidification or diffusionless solidification was also observed when undercoolings are above the critical value. But, how the critical undercooling related to the solidus or T_0 temperature of the alloy was not studied.

In rapid solidification of alloys, such as melt spinning and additive manufacturing (AM), where large undercooling and high growth velocity are possible, the switching between solute diffusion-controlled and thermal diffusion-controlled solidification growth may happen. The switching of control mechanisms is manifested by the variation of microstructural patterns. For instance, Chu *et al.* [11,12] reported dramatic microstructure variation in the Al-2 wt. % Fe melt-spun ribbon, from microcellular on the chill side to coarse cellular on the air side. It is found that the observed sharp microstructural change is due to the switching of the control mechanisms [13]. In AM of alloys, the switching of control mechanisms is also possible. As the solidification rate eventually catches the moving speed of the heat source, the solidification front becomes completely thermal diffusion controlled. In addition, layered microstructures across the melt pool appear in numerous alloys [14–29], indicating a sudden change or changes of the controlling variables during the solidification in AM. However, whether the switching of control mechanisms happens in the AM and how it affects the formation of microstructural patterns is unanswered, which may be due to the experimental difficulties in measuring temperature, solute concentration, and velocity of the interface *in situ*.

In this paper, we focus on the dynamics of the solidification front and investigate if the switching of control mechanisms occurs and how it affects the development of microstructures during the solidification in metal AM. Since almost none of the critical variables of the solidification front can be monitored directly, this research is led by computational modeling and assisted by *in situ* measurement of growth velocity and *ex situ* microstructure characterization. The rest of the paper is structured as follows. Section II briefly introduces the phase-field model employed and how the solidification of the melt pool is modeled. Then, the model is tuned to the *in situ* x-ray imaging experiment and validated against AM experiments of an Al-Si alloy in Sec. III A. The variation of the control variables during the entire solidification process is revealed, and the switching of control mechanisms at the solidification front is confirmed. In Sec. III B, the switching of control mechanisms is further analyzed using Al-4 at. % Cu as an example. Then, the layered structures observed in AM and how they are related to the switching of control mechanisms are discussed. Finally, Sec. IV concludes the findings.

II. PHASE-FIELD MODEL AND SYNCHROTRON X-RAY IMAGING EXPERIMENT

A. Phase-field modeling of rapid solidification

In this study, we employed a phase-field model of rapid solidification for dilute binary alloys with coupled solute and thermal diffusion [30]. The governing dynamic equations in one dimension are given by [30–32]

$$\tau\frac{\partial\phi}{\partial t} = W^2\nabla^2\phi + \phi - \phi^3 - \lambda \times(\theta + Mc_\infty U)(1-\phi^2)^2, \quad (1a)$$

$$\frac{1+k-(1-k)\phi}{2}\frac{\partial U}{\partial t} = \vec{\nabla}\cdot\left(D_l\frac{1-\phi}{2}\vec{\nabla}U + \vec{j}_{at}\right) + \frac{1+(1-k)U}{2}\frac{\partial\phi}{\partial t}, \quad (1b)$$

$$\frac{\partial\theta}{\partial t} = \alpha\nabla^2\theta + \frac{1}{2}\frac{\partial\phi}{\partial t}, \quad (1c)$$

where ϕ is the order parameter denoting liquid ($\phi = -1$) and solid phase ($\phi = 1$), t is time, $\theta = \frac{T-T_M-mc_\infty}{L/c_p}$ is the dimensionless undercooling, T is the temperature field, T_M is

TABLE I. Material properties used in phase-field simulations.

Parameters	Al-4 at. % Cu	Al-11.28 wt. % Si
Melting temperature for pure solvent T_M (K)	933.47[a]	933.47[a]
Equilibrium partition coefficient k_e	0.212[a]	0.2473[a]
Equilibrium liquidus slope m (K/wt%)	−3.465[a]	−8.627[a]
Nominal composition c_∞ (wt%)	8.94	11.28
Latent heat L (J/m^3)	9.47×10^8 [37]	1.07×10^9 [38]
Heat capacity c_p (J/k/m^3)	2.81×10^6 [18]	2.40×10^6 [39]
Interfacial energy γ (J/m^2)	0.158 [40]	0.158 [40]
Capillary length $d_0 = \gamma T_M c_p / L^2$ (m)	4.63×10^{-10}	3.902×10^{-10}
Solute diffusivity in liquid D_l (m^2/s)	3.0×10^{-9} [41]	4.45×10^{-9} [39]
Thermal diffusivity α (m^2/s)	6.23×10^{-5} [42]	3.7×10^{-5} [41]
Diffusion velocity for solute trapping v_D^{PF} (m/s)	2.0 [43]	1.51[b]
Phase-field mobility M_ϕ (m^3/J/s)	5	0.5
Interface thickness δ (m)	5×10^{-9}	5×10^{-9}

[a]Fitted to binary-phase diagrams generated by THERMO-CALC using TCAL7 database.
[b]Determined by fitting to continuous growth model [5,6] [Eq. (2)] using $v_D = 6.52$ m/s [39].

the melting temperature of pure solvent, m is the liquidus slope of the dilute alloy phase diagram, c_∞ is the nominal concentration of the alloy, L is the latent heat, c_p is the specific heat at constant pressure, $U = \frac{1}{1-k}[\frac{2c/c_\infty}{1+k-(1-k)\phi} - 1]$ is the dimensionless concentration, c is the concentration of solute atoms, k is the partition coefficient, α is the thermal diffusivity (assumed the same for both liquid and solid), D_l is the solutal diffusivity in the liquid, $\vec{j}_{at} = a_t W[1 + (1-k)U]\frac{\partial\phi}{\partial t}\frac{\vec{\nabla}\phi}{|\vec{\nabla}\phi|}$ is the antitrapping current [33,34], $\lambda = \frac{15L^2}{16Hc_pT_M}$ is a coupling constant, $H = 3\gamma/\delta$ is the height of the energy barrier for the energy double well, γ is the interfacial energy, δ is the interface thickness, $M = -\frac{m(1-k)}{L/c_p}$ is the scaled magnitude of the liquidus slope, m is the liquidus slope of the dilute alloy phase diagram, $\tau = 1/(HM_\phi)$ is the relaxation time, M_ϕ is the phase-field mobility related to the movement of the interface, and W is related to the width of the diffuse solid-liquid interface [35] (in this work we chose $W = \delta/2\sqrt{2}$).

To consider the solute-trapping effect, a_t in the antitrapping current term $\vec{j}_{at}$ is set to be dependent on ϕ, i.e., $a_t = \frac{1-A(1-\phi^2)}{2\sqrt{2}}$, where $A = \frac{D_L}{v_D^{PF}W}$ is the trapping parameter [36]. v_D^{PF} can be numerically calculated by solving the transcendental relationship between interface velocity v_n and nonequilibrium partition coefficient $k(v)$ [36]:

$$k(v) = k_e \exp\left(\frac{\sqrt{2}(1 - k(v_n))v_n}{v_D^{PF}}\right). \quad (2)$$

The parameters used in this study are listed in Table I. The only unknown parameter is the phase-field mobility M_ϕ, which can be determined by fitting to the measured velocity of the solid-liquid interface. The detailed numerical testing, validation, and exploration of interface kinetics, solute trapping effect, and thermal diffusion of this model can be found in literature [30] and its Supplemental Materials.

In this study, we focus on the dynamics of solid-liquid interface and how it produces the microstructure during the entire solidification of a melt pool. It should be noted that the fusion-type AM process is very complicated and involves many physical processes in different length scales. The interface dynamics, which is our focus in this study, is a physical event happening at the microscopic scale. The AM process is also accompanied by many mesoscale physical processes, such as dynamics of the heat source and its interaction with the powders, the 3D flow effects driven by temperature, surface tension, Marangoni convection, and recoil pressure, surface cooling, and so on. Considering all those phenomena in one multiscale multiphysics model is desirable. However, the model will become extremely complex [44–46], and the linkage between microscopic and mesoscale phenomena will be very challenging. In addition, the physics of a microscopic phenomenon, such as the switching of control mechanisms, may become difficult to separate from such a complex model for further study. Therefore, those mesoscale phenomena are neglected in this study due to their limited impacts on the interface dynamics at the microscopic length (a few nanometers) and time scale (less than 1 μs).

To compare with experiments, we chose to study the resolidification of the melt pool in Al-4 at. % Cu thin film and the resolidification of the melt pool in Al-11.28 wt. % Si bulk. To better capture the essential physics of the microstructural evolution during the entire solidification process, we used a hemisphere and a circle to approximate the geometries of the melt pools in the bulk [3D, Fig. 2(a)] and in the thin film [2D, Fig. 2(b)], respectively. The melt-pool center is the center of the circle or the center of the hemisphere (denoted as the origin O). The melt-pool boundary is the circumference of the circle or the outer surface of the hemisphere. Hence, both simulations can be performed in 1D using a spherical coordinate system, which dramatically lowers the computational cost while still capturing the physics.

In this 1D model, the heat flow is predominantly along the radial direction pointing to the melt-pool boundary as illustrated in Fig. 2(b). Since the growth direction is antiparallel to the direction of heat flow due to the substantial thermal gradient, the growth front moves from the melt-pool boundary to the melt-pool center along the radial direction. Thus, the dynamics of the solid-liquid interface can be captured in 1D. It should be noted that the solid-liquid interface described by this 1D model is the growth front or the solidification front.

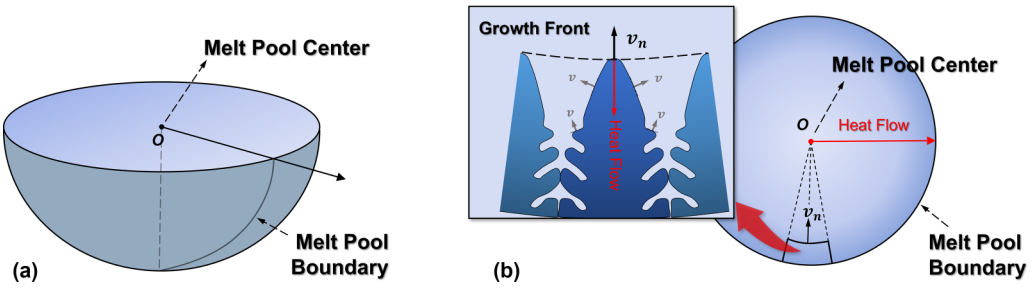

FIG. 2. Phase-field model setup. (a) Three-dimensional schematic of hemispherical melt pool. (b) Top view of melt pool, and zoom-in of growth front and solidifying dendrites with velocity of v_n. Major heat-flow direction is pointing out to melt-pool boundary radially.

As illustrated in Fig. 2(b), the velocity of the growth front is the same as the interface velocity of the primary dendrite tip (or cell tip for cellular structures). The velocities of the side interface of the primary dendrites or cells as well as those of the secondary branches are different from the velocity of the growth front v_n. The temperature and solute composition of those interfaces are also different from those at the growth front. The dynamics of those interfaces controls the formation of grain boundaries, microsecregation, formation of interdendritic phases, and so on. To fully describe those interfaces and the resulting microstructures, 2D or 3D models with anisotropic kinetics and anisotropic interfacial energies are needed. In this work, we focus on the dynamics of the growth front and the formation of the primary solid phase, which forms the skeleton of the final microstructure. Therefore, we ignore the interfaces behind the solidification front because they have minimum influences on the dynamics of the growth front. As will be discussed in the following sections, this 1D model is sufficient to capture all the ncecessary characteristics of the rapid solidification to explain the development of the observed microstructures.

B. Synchrotron x-ray imaging of the solidification front

A high-speed, high-resolution hard x-ray imaging experiment was conducted at beamline 32-ID-B of the Advanced Photon Source at Argonne National Laboratory (Lemont, IL). The primary objective of the experiments was to investigate the real-time dynamics of the melt pool and solidification rate. In the *in situ* experiments, AlSi10Mg plates, with a dimension of 40 mm long × 3 mm wide × 1.1 mm thickness, were used. The electron beam with an accelerating voltage of 60 keV, emission current of 1.8 mA (power of 108 W), beam size of 200 μm and duration time of 3 ms was utilized to perform spot melting on AlSi10Mg substrate. The experiment is to simulate the cooling condition in the powder-bed fusion process under conduction-mode melting in the transverse cross section. The melt pool is also designed to match the simulation domain shape, i.e., a hemisphere-shaped melt pool generated by spot melting. More details about the synchrotron x-ray experiment can be found in previous publications [47–50].

Figure 3 presents a comprehensive outline of the methodology employed to track the solid-liquid interface and determine the solidification rate during solidification of AlSi10Mg using high-speed x-ray imaging. The depth (∼ 194 μm) and width (∼ 227 μm) of the generated melt pool shown in Fig. 3 are comparable to the depth and width of the transverse cross section of the melt pool observed in the powder-bed fusion process [14,15]. In order to calculate the solidification rate, an initial image-processing step was conducted using IMAGEJ, following the approach described in Ref. [48]. This image-processing step aimed to enhance the visibility of the melt-pool boundary. Figure 3(a) shows a representative processed x-ray image during the solidification process, where the solid-liquid interface is prominently discernible.

The tracking of the solid-liquid interface was accomplished by manually tracing the interface at each timeframe, employing a set of discontinuous scattered points. A ninth-order polynomial equation was used to fit these discontinuous scattered points to obtain a fitted curve to represent the solid-liquid interface. Subsequently, the normal direction at any specific point along the solid-liquid interface was determined by calculating the first-order differentiation of the ninth-order fitted curve, as depicted in Figs. 3(b) and 3(c). The solidification rate is then determined by taking the distance the solid-liquid interface travels divided by the corresponding time it takes to cover that distance. This calculation can be expressed using the following equation:

$$v_i = \frac{d_i}{t_i - t_{i-1}}, \tag{3}$$

where i is the interface of interest, v_i is the solidification rate of interface i, and d_i is the distance the solidification front travels from time t_{i-1} to time t_i. The v_i corresponds to the v_n in Fig.2. The time interval between two frames used for calculating the solidification rate is 40 μs.

C. Tuning the phase-field model

To compare with the synchrotron x-ray imaging experiment, the setup of the phase-field simulation is as follows. Al-10Si is used as the binary approximation to AlSi10Mg since Mg stays in the solid solution phase during the solidification and may only form secondary solid phase in the interdendritic region in the final stage of the solidification. The thermal boundary condition applied at the melt-pool center is no flux. At the melt-pool boundary, an interfacial thermal conduction boundary condition is enforced, i.e., $-K\frac{\partial T}{\partial x} = -h(T - T_\infty)$, where $K = \alpha c_p$ is the thermal conductivity, $h = 1.5 \times 10^6$ W m^{-2} K^{-1} is the heat-transfer coefficient [51], and $T_\infty = 300$ K is the temperature of the substrate. No-flux boundary condition is applied to both θ (normalized temperature) and U (normalized composition). The mesh size

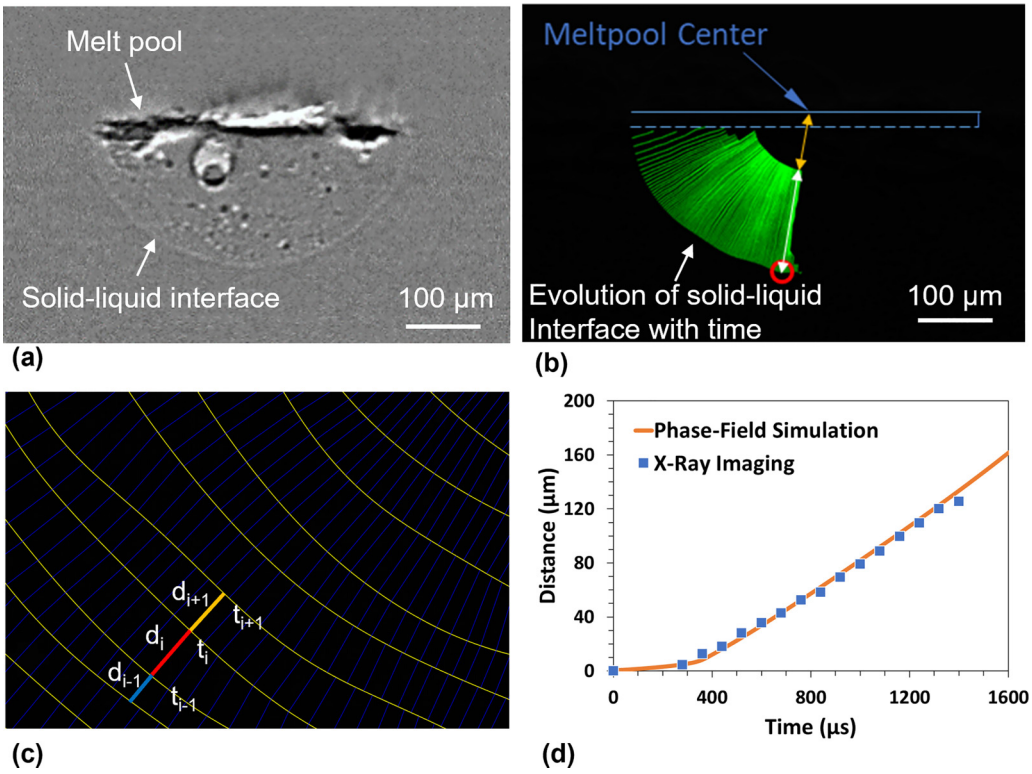

FIG. 3. Solid-liquid interface evolution and method for determining solidification rate. (a) Representative processed x-ray image showing melt pool and solid-liquid interface during solidification of AlSi10Mg. (b) The moving trajectories of the points on the solid-liquid interface along the normal direction (indicated by green lines). (c) Growth trajectories of the solid-liquid interface from t_{i-1} to t_{i+1} during the solidification process. The yellow line indicates solid-liquid interface. (d) Position of solidification front (distance from melt-pool boundary) as a function of time. The phase-field simulation is compared with the x-ray imaging experiment. Uncertainty for melt-pool measurement is 2%.

dx is chosen to be 0.8 W, and the overall simulation size is 150 000 dx (equivalent to 212 μm), which is very close to the melt-pool size of the experiment (the radii of semimajor and semiminor axes are 227 and 194 μm, respectively). The time step dt is 0.01τ.The simulation starts with a uniform temperature of 1200 K and uniform composition $c_\infty = 10$ wt. % Si in liquid state ($\phi = -1$). Once the melt-pool boundary reaches liquidus temperature, a tiny portion at the melt-pool boundary is set to be solid ($\phi = 1$) to mimic the conditions for epitaxial growth, a typical solidification mode in AM [52]. The simulation completes when 99.9% simulation domain is solidified.

Figure 3(d) compares the position of the solidification front as a function of solidification time from both synchrotron x-ray imaging and tuned phase-field simulation. Due to the difficulty in determining the starting point of the solidification, which has a very small initial velocity, a 200-μs offset (10 frames) is applied. The phase-field mobility is found to be around 0.5 $m^3/J/s$.

III. ANALYSIS AND DISCUSSION

A. The resolidification of a melt pool in Al-11.28 wt. % Si

To understand the development of microstructures during AM, we simulated the resolidification of a melt pool of Al-11.28 wt. % Si, which has been studied experimentally [22]. The simulation setup is the same as in Sec. II C, except for the alloy composition, $c_\infty = 11.28$ wt. % Si. The tuned phase-field mobility ($M_\phi = 0.5$ $m^3/J/s$) for AlSi10Mg in Sec. II C is used for this alloy because of their similarity in the alloy composition. The simulation results of the solidification front throughout the entire solidification of the melt pool and the microstructure from experimental observations are compared in Fig. 4.

As shown in the middle panel of Fig. 4(f), the solidification of the simulated melt pool consists of a low-velocity stage and a high-velocity stage. At the beginning of the first stage, the temperature of the solidification front decreases dramatically, while the growth velocity remains low (~ 0.02 m/s). The composition of the solid phase is lower than the alloy composition due to solute partitioning. Therefore, the initial stage is solute diffusion controlled.

When the interfacial temperature drops below a critical temperature, the interface velocity increases significantly [see the sharp increase of the velocity in the middle panel of Fig. 4(f)]. The sudden increase of the velocity leads to the rapid release of latent heat and, consequently the increase of interfacial temperature, i.e., the recalescence. Then, the solidification enters the second stage with a much higher velocity and relatively constant temperature. The composition of the solid phase is the same as the alloy composition, suggesting a diffusionless solidification occurs at the solidification front. As shown in the top panel of Fig. 4(f), the temperature of the solidification front is lower than the solidus, which indicates the growth is now controlled by thermal diffusion. This is scenario (2) discussed in thermodynamic analysis in Sec. I, where

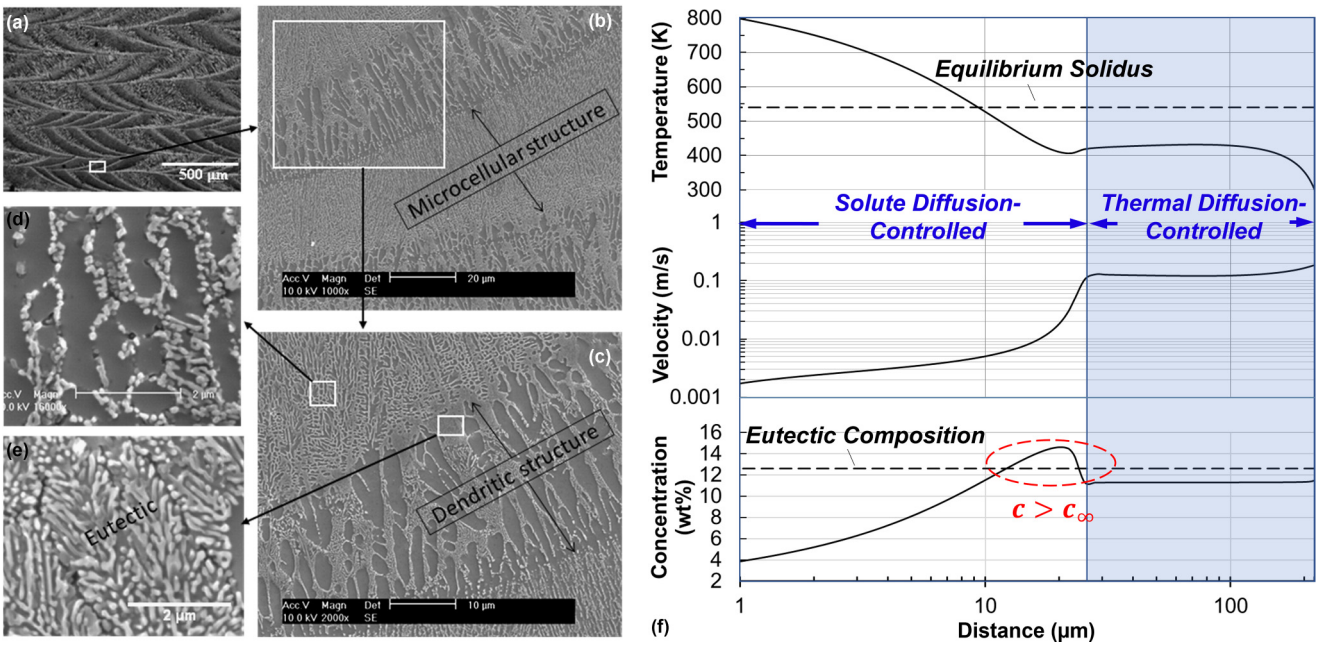

FIG. 4. Microstructure development of melt pools for hypoeutectic Al-Si alloy with composition close to eutectic point. (a)–(e) Scanning Electron Microscopy (SEM) micrographs showing columnar dendrites and microcellular morphology at different points of sample in laser-deposited Al-11.28% Si (reproduced with permission from Ref. [22]). (f) Phase-field simulation of Al-11.28% Si. Calculated instantaneous concentration (wt. %) of solid side of interface, interfacial temperature, and interface velocity are plotted as functions of distance to melt-pool boundary. Inset is setup of phase-field simulation of hemisphere melt pool in 1D spherical coordinates with interfacial thermal conduction on left boundary and nonflux boundary condition on right.

the system lies in the single α-phase region. The predicted growth velocity of this stage ($0.1 \sim 0.2$ m/s) is similar to the experimental measurement from a selected laser-melting study on AlSi10Mg [39]. This rapid increase in velocity is expected to cause sudden refining of the microstructures and consequently develop a sharp boundary separating coarse and fine structures. In the laser-deposited Al-11.28 wt. % Si samples, a clear two-layer structure was observed as shown in Figs. 4(a)–4(c). The coarse dendritic structure developed near the melt-pool boundary, followed by a clear transition to finer dendritic/microcellular structures. The width of the coarse structures developed in the initial stage depends on the cooling rate enforced at the initial boundary of the melt pool. For this simulation, the width is about 20 μm, which is consistent with the observed coarse band in the AM of AlSi10Mg [14,15] and Al-11.28 wt. % Si [Figs. 4(b) and 4(c)] [22].

The phase-field simulation also predicted a composition variation in the resulting solid, as shown in the bottom panel of Fig. 4(f). The predicted solute concentration becomes higher than the alloy composition c_∞ as the solidification approaches the end of the first stage (or getting close to the boundary of the coarse band). The calculated peak solute concentration is even higher than the eutectic composition (12.6 wt. % Si), which may trigger eutectic growth mode. This prediction is also confirmed experimentally in the laser-deposited Al-11.28% Si alloy [22]. As shown in Figs. 4(c) and 4(e), colonies of fine eutectic structures are observed next to the band of microcellular structures. The size of those eutectic colonies is about 5 μm wide, consistent with the phase-field predictions.

In summary, the resolidification of the entire melt pool of Al-11.28 wt. % Si is simulated using the tuned phase-field model. The evolution of the controlling variables (velocity, temperature, and composition) at solidification front are consistent with the microstructures observed in the laser deposition experiment of Al-11.28 wt. % Si [36]. Combining the phase-field simulation results and the microstructure observed experimentally, the following conclusions can be made: (1) the whole solidification process at the solidification front can be naturally divided into solute diffusion-controlled initial transient and thermal diffusion-controlled steady-state stage; (2) the switching of control mechanisms leads to a significant velocity jump, which results in the formation of layered structures; and (3) a slight increase in the solute concentration is also observed near the end of the first stage, which leads to the formation of eutectic colonies between the two layers.

B. The resolidification of Al-4 at. % Cu thin film

To further understand the switching of control mechanisms in the rapid solidification of alloys, we focus on the resolidification of aluminum alloy thin films in this section. Due to the limitations of current characterization techniques, the experimental studies that capture the dynamics of the solid-liquid interface during rapid solidification are rare. Among those interface variables, only the velocity of the solidification front can be measured using *in situ* x-ray imaging [53] or *in situ* transmission electron microscopy (TEM) [54]. Recently, McKeown *et al.* studied rapid solidification dynamics of pulsed laser-melted Al-Cu and Al-Si thin film

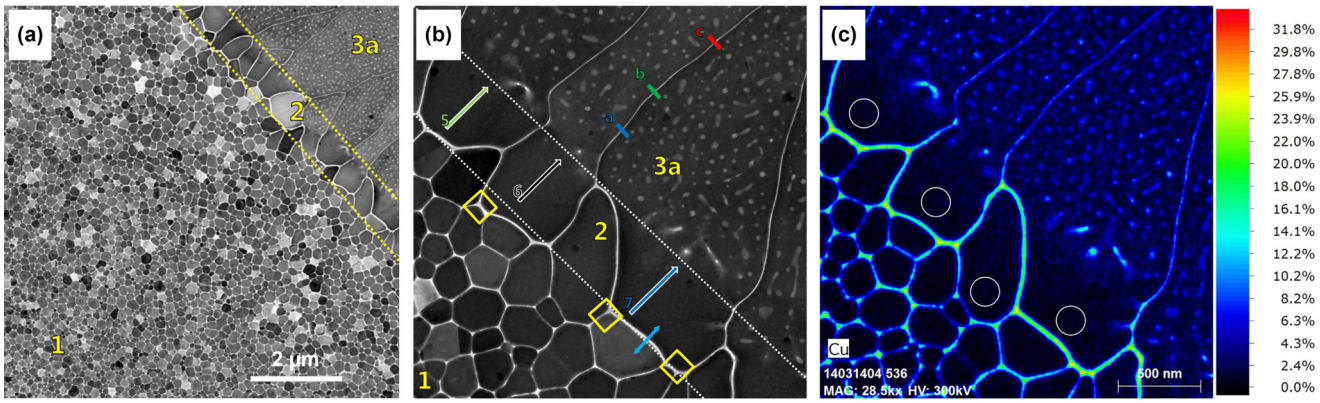

FIG. 5. Optical micrograph of pulsed laser-induced melt pool of Al-4 at. % Cu alloy thin film. (a) Morphologically distinct microstructural zones of solidification microstructure are marked by labels 1, 2, and 3a, respectively. (b) STEM high-angular annular dark-field (HAADF) image of heat-affected zone (zone 1), transition zone (zone 2), and cellular or columnar rapid solidification growth zone (zone 3a). (c) Cu composition heat map of (b) from 0 at. % Cu (dark blue) to 33 at. % Cu (red). (Reproduced with permission from Ref. [56].)

alloys using *in situ* TEM with high spatial and temporal resolution [55–59]. The solidification front was directly observed during the solidification, enabling measurements of the evolving interface velocity. In addition, they found that the developed microstructure has two to three zones with distinct microstructural features, including grain morphology, solute composition, and phases. Figure 5 shows those microstructural features of a rapidly solidified Al-4 at. % thin film [56]. In this section, we used Al-4 at. % Cu thin film as an example to investigate the dynamics of the solidification front during the entire solidification process by phase-field modeling. Followed by the validation with experimental observations [56,57], we show that the solidification growth switched from solute diffusion-controlled to thermal diffusion-controlled, and how it leads to the formation of observed zones with distinct morphologies.

In the phase-field simulation, we used a circle to approximate the true elliptical laser-induced melt pool [56–58]. As illustrated in Fig. 2(a), the origin O is the center of the melt pool, and the circumference is the melt-pool boundary. The whole system was simulated in 1D using a spherical coordinate system. In the simulation, the mesh size dx is chosen to be 0.8 W, and the total simulation size is 35356 dx (equivalent to 50 μm). The time step dt is 0.01τ. The thermal boundary condition of the center of the melt pool is no flux. On the other end of the simulation domain, which is the boundary of the melt pool, a fixed cooling rate is applied. No-flux boundary condition is applied to both θ (normalized temperature) and U (normalized composition) on both ends of the simulation domain. The simulation starts with a uniform temperature of 1200 K and uniform composition $c_\infty = 8.936$ wt. % Cu (equivalent to Al-4 at. % Cu). A small solid seed ($\phi = 1$) is placed on the melt-pool boundary, and the rest of the simulation domain is set as liquid ($\phi = -1$). The simulation completes when 99.9% simulation domain is solidified.

Since the best thermal boundary condition for simulating the resolidification of the melt pool in a thin film is unknown, we tried three cooling rates of different magnitudes (10^6, 10^7, and 10^8 K/s) on the melt-pool boundary to find the best fit. Figure 6(a) shows the evolution of the growth velocity as the interface propagates from the melt-pool boundary to the melt-pool center for each cooling rate. A clear velocity jump is shown in each interface velocity curve. Correspondingly, the temperature of the solid-liquid interface shows a rapid decrease followed by a clear plateau or a slow decline. Those evolutions of the interface indicate a clear two-stage growth behavior, leading to a sharp transition in resulting microstructural features. From the width and velocity of those two stages, we believe that the two stages correspond to zone 2 and zone 3 defined in the experimental work [56–58] (as illustrated in Fig. 5), respectively.

For relatively low cooling rates (10^6 K/s), the profiles of the interface temperature show clear recalescence at the end of the initial transient. This is due to the abrupt increase in the growth velocity, which significantly accelerates the production rate of latent heat and consequently heats up the interface, causing the recalescence. Then, the growth velocity slows down due to the higher interface temperature or lower undercooling. Therefore, the recalescence is followed by a decline in the growth velocity as shown in the lower panel of Fig. 6(a). It should be noted that the decline in velocity after the initial abrupt jump was also observed in the resolidification experiment of Ti6Al4V [60]. At higher cooling rates, above 10^7 K/s, no clear recalescence is observed because all the heat diffuses quickly to the solid side. After the decline, a slight increase in the velocity near the end of the solidification is also observed in each growth-velocity plot. Similar increase in velocity was also shown in laser-remelting Al-Cu experiments [56,59] and Ti6Al4V experiment [60]. This increase is a result of the geometry effect. Due to the decreasing interfacial area of the solidifying circular thin film, the growth velocity must increase to generate enough latent heat to meet the fixed cooling-rate requirement on the melt-pool boundary.

As shown in Fig. 6(b), the cooling rate of 10^7 K/s shows a better agreement with measured velocity [58]. (Since the major and minor axes of the ellipsoid are not equal, we normalized the size of the melt pool for a better comparison.) Hence, we chose the results of 10^7 K/s in the following analysis and discussion.

Figure 6(c) shows the evolution of the solid composition and interface velocity as the growth front moves from the

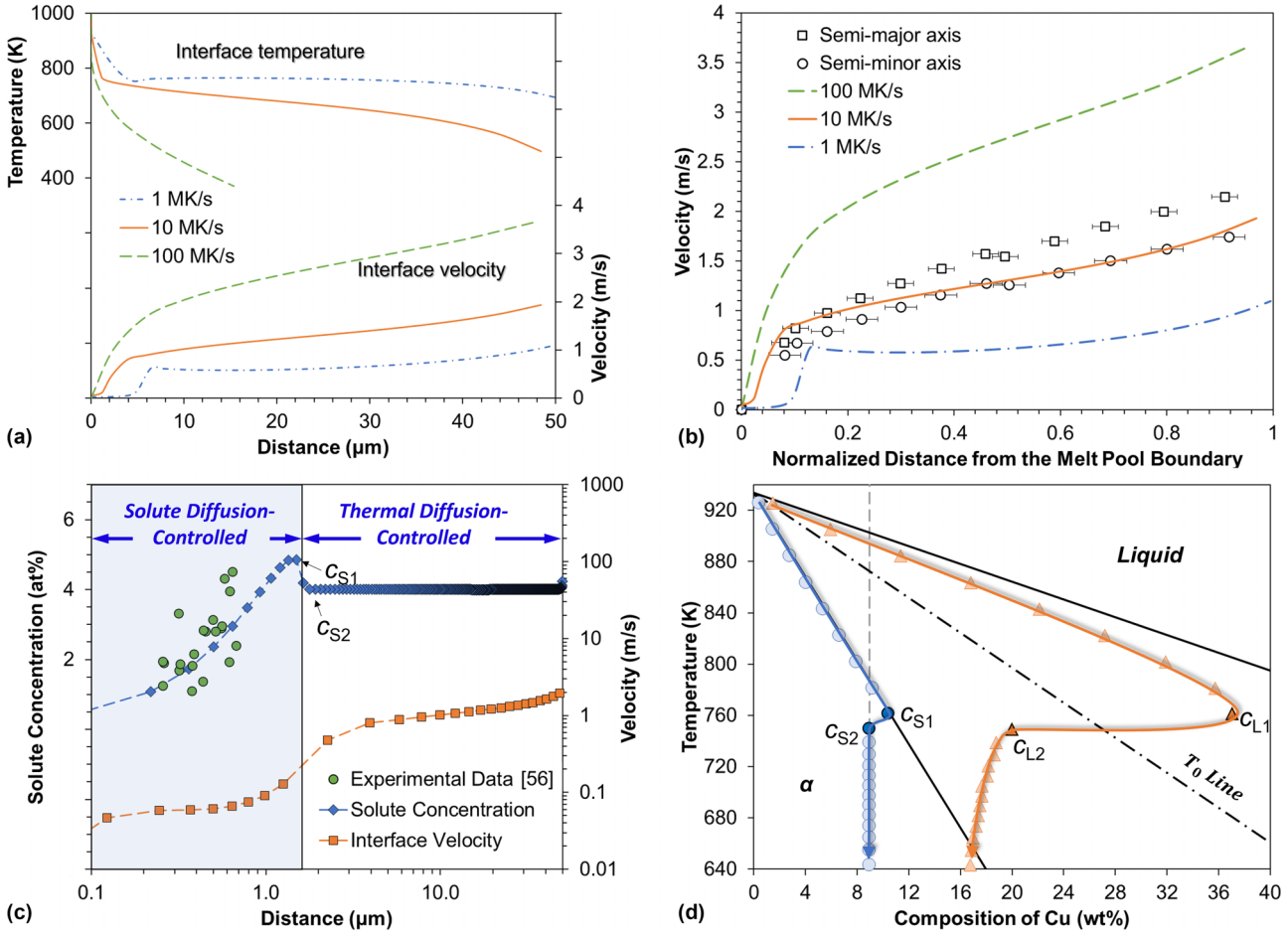

FIG. 6. Evolution of temperature, velocity, and solute concentration at solidification front during resolidification of melt pool in Al-4 at. % Cu thin film simulated by phase-field model. (a) Interface temperature and interface velocity vs distance from melt-pool boundary with different cooling rates. (b) Comparison of measured growth velocities of both semimajor and semiminor axes [58] with simulations. For better comparison, size of melt pool is normalized. (c) Evolution of solute concentration and growth velocity as interface moves from melt-pool boundary to center with cooling rate of 10^7 K/s enforced at melt-pool boundary. Measured solute concentration [56] shows good agreement with simulation. (d) Solute concentrations on both sides of solid-liquid interface as melt pool solidifies with cooling rate of 10^7 K/s enforced at melt-pool boundary. Solid lines are guide for eyes.

melt boundary to the melt-pool center. The width of the first stage is about 2 μm, which agrees well with size of zone 2 (shown in Fig. 5) [56]. The calculated solute concentration profiled in the first stage also agrees well with the measured solute composition along the radial direction in zone 2 of the melt pool [56]. Those pieces of evidence further prove the credibility of our phase-field simulations.

Figure 6(d) shows the evolution of temperature and compositions on both sides of the solidification front from the simulation with the cooling rate of 1×10^7 K/s enforced at the melt-pool boundary. Together with the interface velocity [Fig. 6(c)], the evolution of the interface during the entire solidification process can be explained as follows. The solidification of the melt pool started from the solid outside the melt-pool boundary. Because the solid has the same crystal structure, almost no undercooling is required for nucleation. Hence, the initial temperature of the interface is exactly the equilibrium liquidus, and the initial interface velocity is zero. The solute concentration on the liquid side follows the equilibrium partition coefficient, which lies on the liquidus line. At this point, the interface is clearly solute diffusion controlled. As the solidification continues, the interface temperature decreases, while the growth velocity increases, which causes solute trapping and reduces the partition coefficient. Hence, a small deviation of the solute concentration on the liquid side of the interface from the liquidus line emerges. The increasing interface velocity also leads to the decrease in the characteristic length of solute diffusion ($l_0 = D_l/v_n$). Consequently, the solute concentration of the solidifying solid keeps increasing and results in a solute-rich band [61], as shown in Figs. 6(c) and 6(d). This explains why the solid concentration can reach as high as c_{S1} ($> c_\infty$). As the interface temperature continues to decrease, the solute concentration on the solid side stops increasing and falls back to the nominal composition, $c_{S2} = c_\infty$. The interface becomes thermal diffusion controlled and the solidification becomes diffusionless (complete solute trapping). Consequently, the solute concentration on the liquid side of the interface sees a quick drop from c_{L1} to c_{L2}. Thus, the interface gets into a steady state with a relatively steady temperature and velocity until it approaches the end,

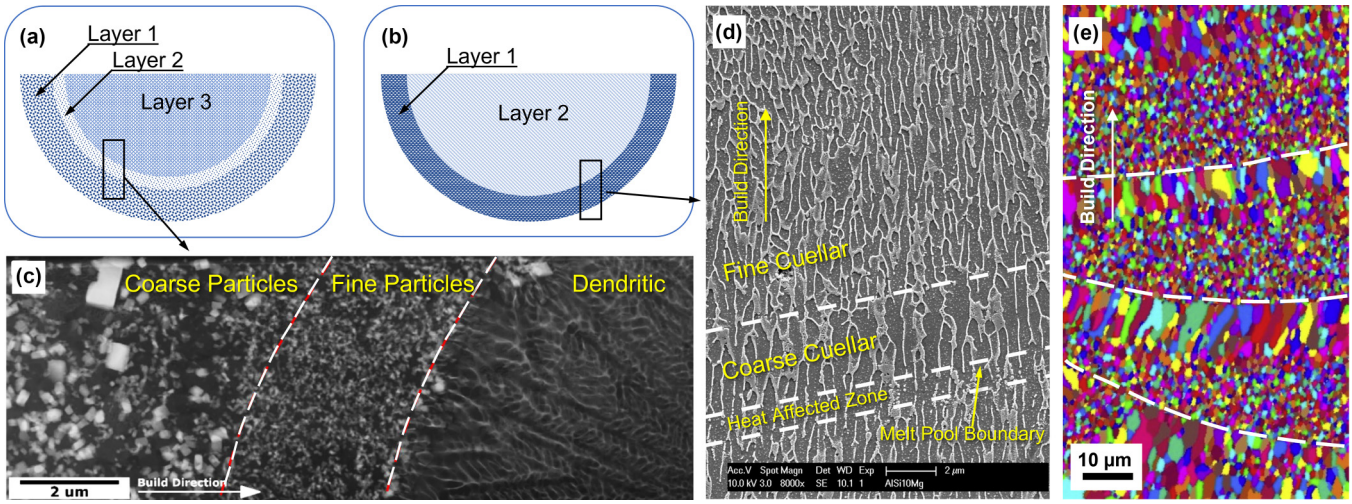

FIG. 7. Layered structures in melt pool. (a) Schematic of three-layered melt-pool structure. (b) Schematic of two-layered melt-pool structure. (c) SEM image of three-layered structure in melt pool of Al-15Ce-9Mg alloy (reproduced with permission from Ref. [23]). (d) SEM image of melt pool in AM-fabricated AlSi10Mg showing coarse-to-fine structural transition (reproduced with permission from Ref. [14]). (d) Bimodal grain structures in AM-fabricated Al-Mg-Zr alloy (reproduced with permission from Ref. [29]).

where an increase in velocity and a decrease in temperature are observed as a result of the geometry effect.

Therefore, it is logical to divide the resolidification of the melt pool into two stages: (I) solute diffusion-controlled initial transient, and (II) thermal diffusion-controlled steady state. The two stages are separated by the rapid increase in growth velocity and a sudden drop in solute concentration. The switching of control mechanisms is caused by the cooling of the interface but not the increase of velocity. Actually, the measured v_D of dilute Al-Cu alloy is 6.7 m/s [3], which is much higher than the measured maximum growth-velocity values [58]. Complete solute trapping in region II is unlikely to happen during the resolidification of the melt pool with a cooling rate less than 10^8 K/s.

C. Layered structures developed in the melt pools of additive manufacturing

From the previous two studies, it can be concluded that switching of control mechanisms happens at the solidification front during the rapid solidification of melt pools. This switching is accompanied by the abrupt change in growth velocity, interface temperature, and solute concentration on both sides of the interface. However, none of those sudden changes can be easily captured *in situ* experimentally, even using the most advanced *in situ* synchrotron x-ray imaging or *in situ* TEM.

In addition, due to the sideways thermal diffusion, the temperature behind the solidification front may be higher than the solidus, especially inside the interdendritic region, leading to the formation of secondary solid phases and solute segregation. [See the high-Cu areas in zone 3a in Fig. 5(b) for example.] Hence, the overall microstructure is complex in both parallel and perpendicular directions to the solidification front moving direction, which makes it challenging to find evidence for the switching of control mechanisms.

Nevertheless, the signature sudden velocity changes due to switching of control mechanisms can still be inferred from the analysis of microstructural features of the as-solidified structures. Since the fineness of the dendrites or microcellular structures is determined by the growth velocity, such abrupt change in growth velocity due to switching of control mechanisms is expected to introduce banded structures in the melt pools with the coarse band next to the melt-pool boundary. Many coarse-fine layered structures similar to Al-11.28 wt. % Si [Figs. 4(a) and 4(b)] are also observed in additively manufactured alloys [Fig. 7(d)] [14,15]. The size of the coarse band depends on the cooling rate as well as the freezing range (difference between liquidus and solidus) of the alloy system. Larger freezing range and slow cool facilitates the formation of larger coarse bands. Therefore, for dilute alloys, which typically have small freezing ranges, the coarse band may be too small to observe.

In addition to the solidification structure change (the fineness), variations in phase selection and grain-structure selection can also be introduced by the evolution in composition, temperature, and velocity at the solidification front during AM, which makes melt-pool structure even more complicated. Various inhomogeneous microstructures with two or three layers or zones inside melt pools are observed. The schematics of those layer-structured melt pools are illustrated in Figs. 7(a) and 7(b). Depending on alloy chemistries and processing parameters, the individual layer may be filled with primary intermetallic particles, eutectic structures, cellular/dendritic structures, or superfine equiaxed grains. Figure 7(c) shows an example of a three-layered structure observed in the melt pool of Al-15Ce-9Mg alloy [23], where a microstructural transition of larger primary particles → finer primary particles → dendritic structure is exhibited. Figure 7(d) shows the bimodal grain structures in the melt pool, which may be a result of the formation of potent nucleating intermetallic particles and the switching of control mechanisms. A summary of those layered structures reported in the literature is shown in Table II. Those inhomogeneous layered structures observed in AM strongly suggest that the complex inhomogeneous microstructure developed in the melt pool during AM processes is generic.

TABLE II. Layered microstructures observed in melt pools of AM.

Alloy systems	AlSi10Mg [14,15], Al-11.28Si [22], Al-2.5Fe [24,25], Al-6Cu-6Ce [26]	Al-Ce [62]	Al-Ce-Mn [27], Al-15Fe [28], Al-11Ce-7Mg [23]	Al-15Ce-9Mg [23]	Sc and/or Zr containing Al alloys [16–21,29]
Layer 1	Coarse cellular/dendritic	Eutectic	Intermetallic particles	Large primary particles	Superfine equiaxed grains
Layer 2	Fine cellular/dendritic	Mixed (eutectic and cellular)	Eutectic	Fine primary particles	Coarser columnar grains
Layer 3	NA	Cellular	NA	Dendritic	NA

From the perspective of alloy development, the formation of those layered structures adds another dimension for microstructure manipulation and property tuning. Suppressing the development of those inhomogeneous layered structures can help to form a uniform microstructure throughout the AM-fabricated component and hence to achieve uniform properties. On the other hand, expanding certain layers may be beneficial for certain applications. For instance, increasing the fraction of those layers containing primary intermetallic particles can improve the material performance at elevated temperatures, which is a major direction of current Al alloy development in the industry. However, the fundamental understanding regarding the complex melt-pool microstructure development in AM represents a significant knowledge gap. The switching of control mechanisms is just one facet of the microstructure development in the rapid solidification of a melt pool. A phase-field model with multisolid phases is needed to further explore the phase selection and grain-structure selection and how they are coupled with solidification-structure selection to influence the final microstructures.

IV. CONCLUSIONS

In this study, we employed a phase-field model calibrated using synchrotron x-ray imaging to explore the microstructure development during the rapid solidification of alloys. It was found that the solidification front of the rapidly solidifying melt pool undergoes a switching from a solute diffusion-controlled initial transient to a purely thermal diffusion-controlled steady state. The thermal diffusion-controlled solidification is caused by the low interface temperature rather than the high interface velocity. The switching of control mechanisms perfectly explains the observed abrupt growth-velocity jump, the increase in solute concentration, the formation of eutectic colonies in a hypoeutectic alloy, and the formation of banded/layered structures in rapid solidification experiments. As many inhomogeneous layered/banded structures emerge in AM, it indicates that the switching of control mechanisms is likely a generic phenomenon for AM processes and can be coupled with other solidification modes to form complex inhomogeneous structures inside a melt pool. Understanding the switching of control mechanisms is the first step to unveiling the complexity of the microstructure development in those additively manufactured alloys. It also opens a horizon for AM alloy design by manipulating the inhomogeneous microstructures to achieve optimized properties. This work is a significant stepping stone towards connecting AM processing to microstructure development, which eventually enables AM to print the desired properties on top of the desired geometries.

ACKNOWLEDGMENTS

This work was supported in part by the ISC Advanced Manufacturing Signature Area seed fund at Missouri S&T, U.S. Department of Commerce (Award ID No. 70NANB21H039), and the National Science Foundation under Grant No. OAC-1919789. This research used resources of the Advanced Photon Source, a U.S. Department of Energy (DOE) Office of Science user facility operated for the DOE Office of Science by Argonne National Laboratory under Contract No. DE-AC02-06CH11357. Dr. M. Chu is thanked for helpful discussion.

The authors declare no competing financial interests.

[1] J. S. Langer, Instabilities and pattern formation in crystal growth, Rev. Mod. Phys. **52**, 1 (1980).

[2] P. Galenko and S. Sobolev, Local nonequilibrium effect on undercooling in rapid solidification of alloys, Phys. Rev. E **55**, 343 (1997).

[3] P. M. Smith and M. J. Aziz, Solute trapping in aluminum alloys, Acta Metall. Mater. **42**, 3515 (1994).

[4] P. K. Galenko and D. Jou, Rapid solidification as non-ergodic phenomenon, Phys. Rep. **818**, 1 (2019).

[5] M. J. Aziz and W. J. Boettinger, On the transition from short-range diffusion-limited to collision-limited growth in alloy solidification, Acta Metall. Mater. **42**, 527 (1994).

[6] M. J. Aziz and T. Kaplan, Continuous growth model for interface motion during alloy solidification, Acta Metall. **36**, 2335 (1988).

[7] J. Baker, and J. Cahn, Solute trapping by rapid solidification, Acta Metall. **17**, 575 (1969).

[8] J. C. Baker and J. W. Cahn, Thermodynamics of solidification, in *The Selected Works of John W. Cahn* (John Wiley & Sons, Inc., Hoboken, NJ, 2013), pp. 253–288.

[9] K. Eckler, R. F. Cochrane, D. M. Herlach, B. Feuerbacher, and M. Jurisch, Evidence for a transition from diffusion-controlled to thermally controlled solidification in metallic alloys, Phys. Rev. B **45**, 5019 (1992).

[10] K. Eckler, D. M. Herlach, R. G. Hamerton, and A. L. Greer, Dendrite growth velocities in highly undercooled, dilute Ni-C melts, Mater. Sci. Eng. A **133**, 730 (1991).

[11] M. G. Chu, A. Giron, and D. A. Granger, Microstructure and heat flow in melt-spun aluminum alloys, in *Proceedings of the ASM's International Conference on Rapidly Solidified Materials* (ASM International, Metals Park, OH, 1986), pp. 311–316.

[12] M. G. Chu and D. A. Granger, Solidification and microstructure analysis of rapidly solidified melt-spun Al-Fe alloys, Metall. Trans. A **21**, 205 (1990).

[13] N. Najafizadeh, M. G. Chu, and Y. Gu, Selection of solidification pathway in rapid solidification processes, Phys. Rev. Mater. **7**, 023403 (2023).

[14] L. Thijs, K. Kempen, J.-P. Kruth, and J. Van Humbeeck, Fine-structured aluminium products with controllable texture by selective laser melting of pre-alloyed AlSi10Mg powder, Acta Mater. **61**, 1809 (2013).

[15] M. Tang, Inclusions, porosity, and fatigue of AlSi10Mg parts produced by selective laser melting, Ph.D. thesis, Carnegie Mellon University, Pittsburgh PA, 2017.

[16] H. Zhang, H. Zhu, X. Nie, J. Yin, Z. Hu, and X. Zeng, Effect of zirconium addition on crack, microstructure and mechanical behavior of selective laser melted Al-Cu-Mg alloy, Scr. Mater. **134**, 6 (2017).

[17] A. B. Spierings, K. Dawson, K. Kern, F. Palm, and K. Wegener, SLM-processed Sc- and Zr- modified Al-Mg alloy: Mechanical properties and microstructural effects of heat treatment, Mater. Sci. Eng. A **701**, 264 (2017).

[18] A. B. Spierings, K. Dawson, T. Heeling, P. J. Uggowitzer, R. Schäublin, F. Palm, and K. Wegener, Microstructural features of Sc- and Zr-modified Al-Mg alloys processed by selective laser melting, Mater. Des. **115**, 52 (2017).

[19] A. B. Spierings, K. Dawson, M. Voegtlin, F. Palm, and P. J. Uggowitzer, Microstructure and mechanical properties of as-processed scandium-modified aluminium using selective laser melting, CIRP Ann. **65**, 213 (2016).

[20] R. Li, M. Wang, Z. Li, P. Cao, T. Yuan, and H. Zhu, Developing a high-strength Al-Mg-Si-Sc-Zr alloy for selective laser melting: Crack-inhibiting and multiple strengthening mechanisms, Acta Mater. **193**, 83 (2020).

[21] J. H. Martin, B. D. Yahata, J. M. Hundley, J. A. Mayer, T. A. Schaedler, and T. M. Pollock, 3D printing of high-strength aluminium alloys, Nature (London) **549**, 365 (2017).

[22] G. P. Dinda, A. K. Dasgupta, and J. Mazumder, Evolution of microstructure in laser deposited Al–11.28%Si alloy, Surf. Coat. Technol. **206**, 2152 (2012).

[23] K. Sisco, A. Plotkowski, Y. Yang, D. Leonard, B. Stump, P. Nandwana, R. R. Dehoff, and S. S. Babu, Microstructure and properties of additively manufactured Al–Ce–Mg alloys, Sci. Rep. **11**, 6953 (2021).

[24] X. Qi, N. Takata, A. Suzuki, M. Kobashi, and M. Kato, Laser powder bed fusion of a near-eutectic Al–Fe binary alloy: Processing and microstructure, Addit. Manuf. **35**, 101308 (2020).

[25] Y. Wu, T. Zhang, C. Chen, S. R. E. Hosseini, X. Zhang, and K. Zhou, Microstructure and mechanical property evolution of additive manufactured eutectic Al-2Fe alloy during solidification and aging, J. Alloys Compd. **897**, 163243 (2022).

[26] S. Bahl, K. Sisco, Y. Yang, F. Theska, S. Primig, L. F. Allard, R. A. Michi, C. Fancher, B. Stump, R. Dehoff, A. Shyam, and A. Plotkowski, Al-Cu-Ce(-Zr) alloys with an exceptional combination of additive processability and mechanical properties, Addit. Manuf. **48**, 102404 (2021).

[27] A. Plotkowski, K. Sisco, S. Bahl, A. Shyam, Y. Yang, L. Allard, P. Nandwana, A. M. Rossy, and R. R. Dehoff, Microstructure and properties of a high temperature Al–Ce–Mn alloy produced by additive manufacturing, Acta Mater. **196**, 595 (2020).

[28] W. Wang, N. Takata, A. Suzuki, M. Kobashi, and M. Kato, Formation of multiple intermetallic phases in a hypereutectic Al–Fe binary alloy additively manufactured by laser powder bed fusion, Intermetallics **125**, 106892 (2020).

[29] J. R. Croteau, S. Griffiths, M. D. Rossell, C. Leinenbach, C. Kenel, V. Jansen, D. N. Seidman, D. C. Dunand, and N. Q. Vo, Microstructure and mechanical properties of Al-Mg-Zr alloys processed by selective laser melting, Acta Mater. **153**, 35 (2018).

[30] Y. Gu, X. He, and D. Han, On the phase-field modeling of rapid solidification, Comput. Mater. Sci. **199**, 110812 (2021).

[31] J. C. Ramirez, C. Beckermann, A. Karma, and H.-J. Diepers, Phase-field modeling of binary alloy solidification with coupled heat and solute diffusion, Phys. Rev. E **69**, 051607 (2004).

[32] J. Rosam, P. K. Jimack, and A. M. Mullis, Quantitative phase-field modeling of solidification at high lewis number, Phys. Rev. E **79**, 030601(R) (2009).

[33] A. Karma, Phase-field formulation for quantitative modeling of alloy solidification, Phys. Rev. Lett. **87**, 115701 (2001).

[34] B. Echebarria, R. Folch, A. Karma, and M. Plapp, Quantitative phase-field model of alloy solidification, Phys. Rev. E **70**, 061604 (2004).

[35] S. G. Kim, W. T. Kim, and T. Suzuki, Phase-field model for binary alloys, Phys. Rev. E **60**, 7186 (1999).

[36] T. Pinomaa and N. Provatas, Quantitative phase field modeling of solute trapping and continuous growth kinetics in quasi-rapid solidification, Acta Mater. **168**, 167 (2019).

[37] J. J. Valencia and P. N. Quested, Thermophysical properties, in *ASM Handbook*, Vol. 15 (ASM International, 2008), p. 468.

[38] P. Wei, Z. Wei, Z. Chen, Y. He, and J. Du, Thermal behavior in single track during selective laser melting of AlSi10Mg powder, Appl. Phys. A **123**, 604 (2017).

[39] M. M. Coday, In-situ X-ray imaging of the selective laser melting process, Master's thesis, Missouri University of Science and Technology, Rolla MO, 2020.

[40] N. Eustathopoulos, L. Coudurier, J. C. Joud, and P. Desré, Tension interfaciale solide-liquide des systémes Al-Sn, Al-In et Al-Sn-In, J. Cryst. Growth **33**, 105 (1976).

[41] W. Kurz and D. J. Fisher, *Fundamentals of Solidification, Fourth Rev.* (Trans Tech Pubilications Ltd., Zurich, Switzerland, 1998).

[42] M. Leitner, T. Leitner, A. Schmon, K. Aziz, and G. Pottlacher, Thermophysical properties of liquid aluminum, Metall. Mater. Trans. A **48**, 3036 (2017).

[43] T. Pinomaa, J. M. McKeown, J. M. K. Wiezorek, N. Provatas, A. Laukkanen, and T. Suhonen, Phase field modeling of rapid resolidification of Al-Cu thin films, J. Cryst. Growth **532**, 125418 (2020).

[44] J. Berry, A. Perron, J.-L. Fattebert, J. D. Roehling, B. Vrancken, T. T. Roehling, D. L. Rosas, J. A. Turner, S. A. Khairallah, J. T. McKeown, and M. J. Matthews, Toward multiscale simulations of tailored microstructure formation in metal additive manufacturing, Mater. Today **51**, 65 (2021).

[45] T. W. Heo, S. A. Khairallah, R. Shi, J. Berry, A. Perron, N. P. Calta, A. A. Martin, N. R. Barton, J. Roehling, T. Roehling,

J.-L. Fattebert, A. Anderson, A. L. Nichols, S. Wopschall, W. E. King, J. T. McKeown, and M. J. Matthews, A mesoscopic digital twin that bridges length and time scales for control of additively manufactured metal microstructures, J. Phys. Mater. **4**, 034012 (2021).

[46] M. M. Francois, A. Sun, W. E. King, N. J. Henson, D. Tourret, C. A. Bronkhorst, N. N. Carlson, C. K. Newman, T. Haut, J. Bakosi, J. W. Gibbs, V. Livescu, S. A. Vander Wiel, A. J. Clarke, M. W. Schraad, T. Blacker, H. Lim, T. Rodgers, S. Owen, F. Abdeljawad, J. Madison, A. T. Anderson, J.-L. Fattebert, R. M. Ferencz, N. E. Hodge, S. A. Khairallah, and O. Walton, Modeling of additive manufacturing processes for metals: Challenges and opportunities, Curr. Opin. Solid State Mater. Sci. **21**, 198 (2017).

[47] M. Qu, Q. Guo, L. I. Escano, A. Nabaa, S. M. H. Hojjatzadeh, Z. A. Young, and L. Chen, Controlling process instability for defect lean metal additive manufacturing, Nat. Commun. **13**, 1079 (2022).

[48] Q. Guo, C. Zhao, M. Qu, L. Xiong, S. M. H. Hojjatzadeh, L. I. Escano, N. D. Parab, K. Fezzaa, T. Sun, and L. Chen, In-situ full-field mapping of melt flow dynamics in laser metal additive manufacturing, Addit. Manuf. **31**, 100939 (2020).

[49] Q. Guo, C. Zhao, L. I. Escano, Z. Young, L. Xiong, K. Fezzaa, W. Everhart, B. Brown, T. Sun, and L. Chen, Transient dynamics of powder spattering in laser powder bed fusion additive manufacturing process revealed by in-situ high-speed high-energy x-ray imaging, Acta Mater. **151**, 169 (2018).

[50] L. I. Escano, S. J. Clark, A. C. Chuang, J. Yuan, Q. Guo, M. Qu, W. Dong, X. Zhang, J. Huang, K. Fezzaa, P. Kenesei, B. J. Walker, T. Sun, K. W. Eliceiri, and L. Chen, An electron beam melting system for in-situ synchrotron x-ray monitoring, Addit. Manuf. Lett. **3**, 100094 (2022).

[51] T. W. Clyne, Numerical treatment of rapid solidification, Metall. Trans. B **15**, 369 (1984).

[52] T. DebRoy, H. L. Wei, J. S. Zuback, T. Mukherjee, J. W. Elmer, J. O. Milewski, A. M. Beese, A. Wilson-Heid, A. De, and W. Zhang, Additive manufacturing of metallic components–process, structure and properties, Prog. Mater. Sci. **92**, 112 (2018).

[53] C. Kenel, D. Grolimund, X. Li, E. Panepucci, V. A. Samson, D. F. Sanchez, F. Marone, and C. Leinenbach, In situ investigation of phase transformations in Ti-6Al-4V under additive manufacturing conditions combining laser melting and high-speed micro-x-ray diffraction, Sci. Rep. **7**, 16358 (2017).

[54] J. T. McKeown, A. J. Clarke, and J. M. K. Wiezorek, Imaging transient solidification behavior, MRS Bull. **45**, 916 (2020).

[55] J. D. Roehling, D. R. Coughlin, J. W. Gibbs, J. K. Baldwin, J. C. E. Mertens, G. H. Campbell, A. J. Clarke, and J. T. McKeown, Rapid solidification growth mode transitions in Al-Si alloys by dynamic transmission electron microscopy, Acta Mater. **131**, 22 (2017).

[56] K. W. Zweiacker, C. Liu, M. A. Gordillo, J. T. McKeown, G. H. Campbell, and J. M. K. Wiezorek, Composition and automated crystal orientation mapping of rapid solidification products in hypoeutectic Al-4 at.%Cu alloys, Acta Mater. **145**, 71 (2018).

[57] J. T. McKeown, A. K. Kulovits, C. Liu, K. Zweiacker, B. W. Reed, T. LaGrange, J. M. K. Wiezorek, and G. H. Campbell, In situ transmission electron microscopy of crystal growth-mode transitions during rapid solidification of a hypoeutectic Al–Cu alloy, Acta Mater. **65**, 56 (2014).

[58] J. T. McKeown, K. Zweiacker, C. Liu, D. R. Coughlin, A. J. Clarke, J. K. Baldwin, J. W. Gibbs, J. D. Roehling, S. D. Imhoff, P. J. Gibbs, D. Tourret, J. M. K. Wiezorek, and G. H. Campbell, Time-resolved in situ measurements during rapid alloy solidification: Experimental insight for additive manufacturing, JOM **68**, 985 (2016).

[59] V. Bathula, C. Liu, K. Zweiacker, J. McKeown, and J. M. K. Wiezorek, Interface velocity dependent solute trapping and phase selection during rapid solidification of laser melted hypoeutectic Al-11at.%Cu alloy, Acta Mater. **195**, 341 (2020).

[60] C. Zhao, K. Fezzaa, R. W. Cunningham, H. Wen, F. De Carlo, L. Chen, A. D. Rollett, and T. Sun, Real-time monitoring of laser powder bed fusion process using high-speed x-ray imaging and diffraction, Sci. Rep. **7**, 3602 (2017).

[61] M. C. Flemings, *Solidification Processing* (McGraw-Hill, New York, 1974).

[62] A. Plotkowski, O. Rios, N. Sridharan, Z. Sims, K. Unocic, R. T. Ott, R. R. Dehoff, and S. S. Babu, Evaluation of an Al-Ce alloy for laser additive manufacturing, Acta Mater. **126**, 507 (2017).

Correction: The omission of a support statement in the Acknowledgment section has been fixed.